Available online at ScienceDirect

Nuclear Engineering and Technology

journal homepage: www.elsevier.com/locate/net

Original Article

Effects of No Stiffness Inside Unbonded Tendon Ducts on the Behavior of Prestressed Concrete Containment Vessels

Sang-Hoon Noh [a,b,*], *Hyo-Gyong Kwak* [c], *and Raeyoung Jung* [d]

[a] *Korea Advanced Institute of Science and Technology, 291, Daehak-ro, Yuseong-Gu, Daejeon 34141, Republic of Korea*

[b] *Korea Hydro & Nuclear Power Co., Ltd, 70, 1312-gil Yuseong-daero, Yuseong-Gu, Daejeon 34101, Republic of Korea*

[c] *Korea Advanced Institute of Science and Technology, 291, Daehak-ro, Yuseong-Gu, Daejeon 34141, Republic of Korea*

[d] *Korea Institute of Nuclear Safety, 62, Gwahak-ro, Yuseong-Gu, Daejeon 34142, Republic of Korea*

ARTICLE INFO

Article history:
Received 17 September 2015
Received in revised form
7 December 2015
Accepted 16 January 2016
Available online 2 February 2016

Keywords:
Containment
Internal Pressure
Prestressed Concrete
Structural Analysis
Structural Integrity
Tendon

ABSTRACT

The numerical simulation methodologies to evaluate the structural behaviors of prestressed concrete containment vessels (PCCVs) have been substantially developed in recent decades. However, there remain several issues to be investigated more closely to narrow the gap between test results and numerical simulations. As one of those issues, the effects of no stiffness inside unbonded tendon ducts on the behavior of PCCVs are investigated in this study. Duct holes for prestressing cables' passing are provided inside the containment wall and dome in one to three directions for general PCCVs. The specific stress distribution along the periphery of the prestressing duct hole and the loss of stiffness inside the hole, especially in an unbonded tendon system, are usually neglected in the analysis of PCCVs with the assumption that the duct hole is filled with concrete. However, duct holes are not small enough to be neglected. In this study, the effects of no stiffness inside the unbonded tendon system on the behaviors of PCCVs are evaluated using both analytical and numerical approaches. From the results, the effects of no stiffness in unbonded tendons need to be considered in numerical simulations for PCCVs, especially under internal pressure loading.

* *Corresponding author.*
E-mail addresses: hoonor@kaist.ac.kr, sanghoon.noh@khnp.co.kr (S.-H. Noh).

http://dx.doi.org/10.1016/j.net.2016.01.008

1. Introduction

Reactor containments might be subjected to high internal pressure under severe conditions such as a loss-of-coolant accident. As a final barrier, the containments have to prevent radioactive materials that can seriously damage public health and welfare from being released to the external environment. Therefore, a containment must be able to sustain its function for its life time.

Most of the containments built in recent decades are of the prestressed concrete containment vessel (PCCV) type. For as long as PCCVs have been designed, built, and monitored, there have been continuous discussions on technical issues including pros and cons between bonded and unbonded tendon solutions in post-tensioning. An important issue under discussion is the reliability of analysis methods and tools to verify design criteria and lifetime behaviors of PCCVs. The methodology to evaluate structural integrity of PCCVs using numerical simulation has been substantially developed with the help of the rapid growth in computational technology [1–5].

However, several issues remain to be investigated closely to narrow the gap between tests and numerical simulations. For example, a numerical analysis to simulate the test results obtained from the structural integrity test (SIT) for a PCCV expected smaller displacements than the measured ones by > 20% at some locations, even though the state-of-the art numerical simulation methodology was used [1]. The gaps of displacements between the SIT and the numerical simulation were relatively high, especially in geometrically noncontinuous regions such as near buttress and near penetrations. Similar gaps between tests and simulations have been reported in previous studies such as International Standard Problem on Containment Integrity (ISP) 48 [2,3].

Studies to improve the methodology to simulate structural behaviors of PCCVs, especially under internal pressure, to minimize the gap between tests and simulations have been performed.

In previous studies, the gaps between displacements from the SIT for a PCCV and displacements from the numerical analyses simulating the test were found to be reduced under consideration of no stiffness effects inside unbonded tendon ducts [4,5].

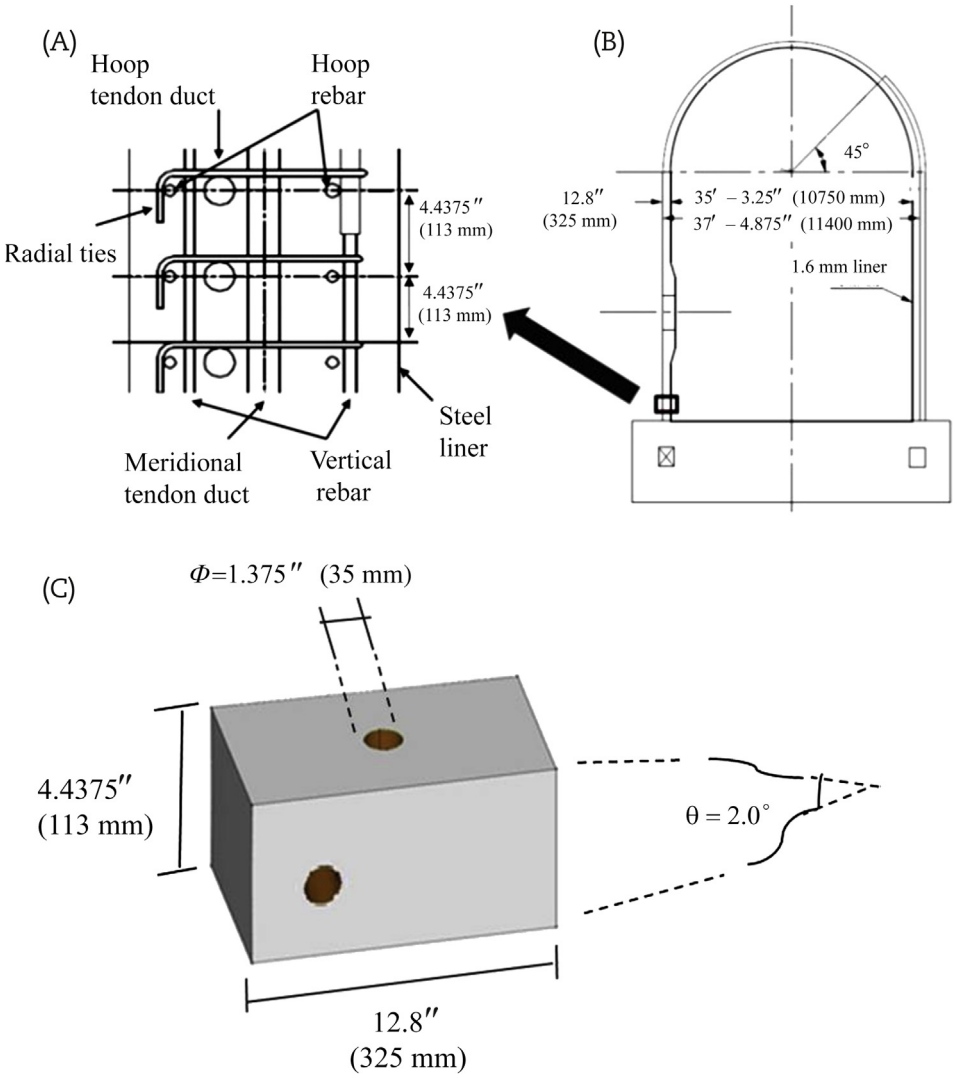

Fig. 1 – The 1:4 scale PCCV model. (A) Typical wall section. (B) 1:4 scale model section. (C) Unit pattern of tendon ducts arrangement in wall. PCCV, prestressed concrete containment vessel.

Following up the previous study in view of displacement, the effects of no stiffness inside an unbonded tendon system on the behaviors of PCCVs, in terms of stress and strain, are evaluated using both analytical and numerical approaches in this study.

2. Theoretical background

2.1. Composition of wall section in a PCCV

The wall section in a PCCV is generally composed of structural members of concrete, rebar, and tendon. There is a steel lining or epoxy coating in the internal section of the wall for leak tightness.

A typical wall section of a 1:4 scale PCCV model with the section of the structure is shown in Fig. 1 [2].

The hoop ducts, through which hoop tendons pass, and the hoop rebars (reinforcement steel) were typically spaced at an interval of 113 mm (4.4375″) along the vertical direction, as shown in Figs. 1A and 1C. The meridional ducts through which meridional tendons pass were typically arranged at an interval of 2°, which corresponds to 193 mm (7.612″) along the centerline of the ducts in the circumferential direction, as described in Fig. 1C.

The ducts were generally 35 mm (1–3/8″) in diameter and were not greased after tensioning in the 1:4 scale model [2], whereas the prototype tendon ducts were, as typical of most unbonded tendons, injected with heavy grease after tensioning to protect the tendons from corrosion. Since the model tendons would be in use only for a relatively short time (< 2 years), they were not greased.

2.2. Stress concentration due to tendon ducts

In general the walls of a PCCV under internal pressure loadings are subjected to biaxial tension in the circumferential and meridional directions.

A diagram of the typical wall section of the 1:4 scale PCCV model under vertical tension due to internal pressure loading, with only concrete, hoop duct, and tendon for simplification, is described in Fig. 2.

As shown in Fig. 2, the space inside ducts is empty except for the space occupied by the hoop tendon that is passing through the ducts. Even though hoop tendons are located inside ducts, those tendons contribute to resistance to external loads only in the circumferential or horizontal direction, and not in the vertical direction, because the only connection between ducts and tendons is friction.

The same explanation of Fig. 2 in the vertical direction can be applied to the case of Fig. 3 in the circumferential direction.

Accordingly, the conditions described both in Figs. 2 and 3 are associated with the problems of plates containing a circular hole under tension.

Stresses in a plate under tension or compression are calculated by the formula $\sigma = P/A$ under ordinary circumstances. This formula is based upon a uniform stress (σ) distribution acting over the cross-sectional area (A) of the plate, and therefore it is valid only for plates that are free from of any changes in geometry (no holes, grooves, or other discontinuities in shape).

Irregularities of holes or other abrupt changes create a disruption in the stress pattern, causing high stresses over a very small region.

Accordingly, the stress (σ_{max}) near a duct hole might be higher than the nominal stress (σ_{nom}) under tension in the problem schematically described in Figs. 2 and 3.

To quantitatively evaluate the stress concentration and the distribution pattern due to tendon duct holes for the cases of Figs. 2 and 3, both the analytical approach based on the *theory of elasticity* [6] and the numerical approach based on the *finite element method* were utilized.

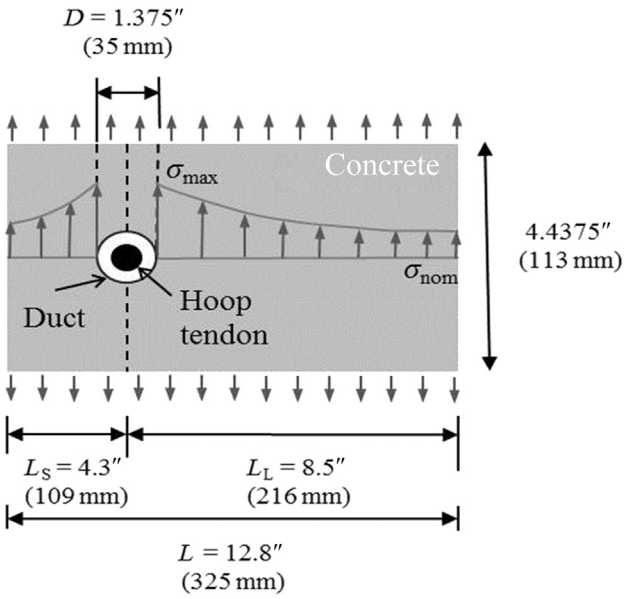

Fig. 2 – Wall section with hoop duct hole under vertical tension.

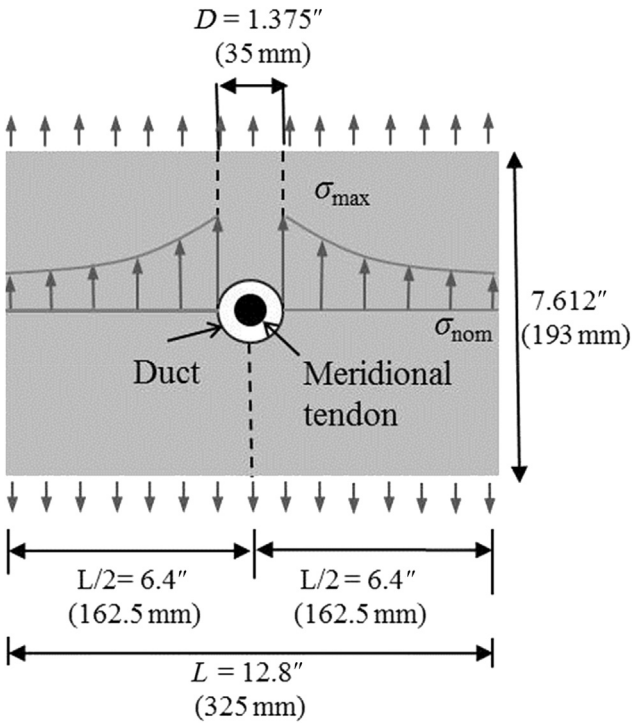

Fig. 3 – Wall section with meridional tendon duct hole under circumferential tension.

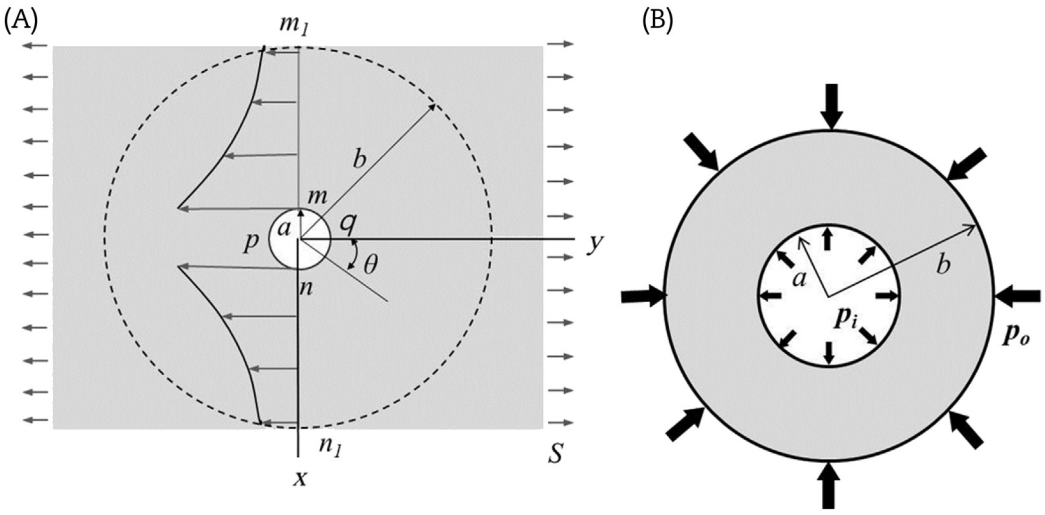

Fig. 4 – Stress distribution diagrams. (A) Plate with a circular hole. (B) Hollow cylinder.

2.3. *Evaluation based on theory of elasticity*

Fig. 4A represents a plate subjected to a uniform tension of magnitude S in the y direction. If a small circular hole is made in the middle of the plate, the stress distribution in the neighborhood of the hole will be changed, but it can be concluded from Saint–Venant's principle [6] that the change is negligible at large distances.

When a portion of the plate within a concentric circle of radius b, which is large in comparison with a, is considered, the stresses at radius b are effectively the same as in the plate without the hole and are therefore given as follows:

$$(\sigma_r)_{r=b} = S\cos^2\theta = \frac{1}{2}S(1+\cos 2\theta) \tag{1A}$$

$$(\tau_{r\theta})_{r=b} = -\frac{1}{2}S\sin 2\theta \tag{1B}$$

where σ_r is the radial normal stress in cylindrical coordinates and $\tau_{r\theta}$ is the shearing stress in cylindrical coordinates.

These forces, acting around the outside of the ring having an inner radius a and an outer radius b, give a stress distribution within the ring, which we may consider as consisting of two parts. The first is due to the constant component ½S of the normal forces. The condition of the first part comes into the problem of a hollow cylinder subjected to uniform pressure on the inner (p_i) and outer (p_o) surfaces, as described in Fig. 4B. Accordingly, the stresses the first part produces can be calculated by means of Eqs. (2A) and (2B) for the solution of the problem of Fig. 4B [6].

$$\sigma_r = \frac{a^2b^2(p_o-p_i)}{b^2-a^2}\frac{1}{r^2} + \frac{p_ia^2-p_ob^2}{b^2-a^2} \tag{2A}$$

$$\sigma_\theta = -\frac{a^2b^2(p_o-p_i)}{b^2-a^2}\frac{1}{r^2} + \frac{p_ia^2-p_ob^2}{b^2-a^2} \tag{2B}$$

where σ_r is the radial normal stress in cylindrical coordinates and σ_θ is the tangential normal stress in cylindrical coordinates.

The remaining part, consisting of the normal forces ½S cos 2θ, together with the shearing forces −½S sin 2θ, produces stresses that may be derived from a stress function of the following form:

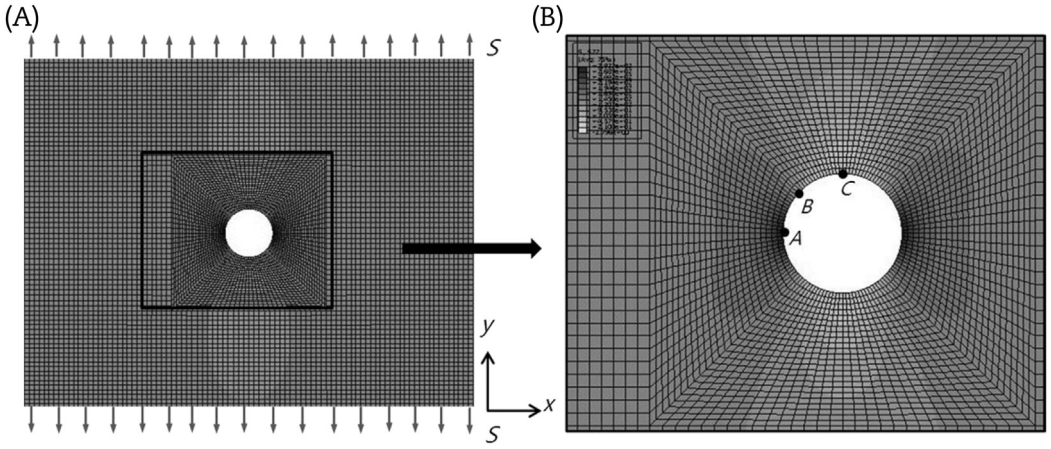

Fig. 5 – Finite element model [9°S] and generated meshes. (A) Concrete elements. (B) Points of comparison.

$$\phi = f(r)\cos 2\theta \tag{3}$$

Substituting this into the compatibility equation, we get:

$$\left(\frac{\partial^2}{\partial r^2}+\frac{1}{r}\frac{\partial}{\partial r}+\frac{1}{r^2}\frac{\partial^2}{\partial \theta^2}\right)\left(\frac{\partial^2\phi}{\partial r^2}+\frac{1}{r}\frac{\partial\phi}{\partial r}+\frac{1}{r^2}\frac{\partial^2\phi}{\partial\theta^2}\right)=0 \tag{4}$$

The following ordinary differential equation is used to determine $f(r)$:

$$\left(\frac{d^2}{dr^2}+\frac{1}{r}\frac{d}{dr}-\frac{4}{r^2}\right)\left(\frac{d^2f}{dr^2}+\frac{1}{r}\frac{df}{dr}-\frac{4f}{r^2}\right)=0 \tag{5}$$

The general solution is as follows:

$$f(r) = Ar^2 + Br^4 + C\frac{1}{r^2} + D \tag{6}$$

The stress function is, therefore,

$$\phi = \left(Ar^2 + Br^4 + C\frac{1}{r^2} + D\right)\cos 2\theta$$

and the corresponding stress components are:

$$\sigma_r = \frac{1}{r}\frac{\partial\phi}{\partial r}+\frac{1}{r^2}\frac{\partial\phi}{\partial\theta^2} = -\left(2A+\frac{6C}{r^4}+\frac{4D}{r^2}\right)\cos 2\theta \tag{8A}$$

$$\sigma_\theta = \frac{\partial^2\phi}{\partial r^2} = \left(2A+12Br^2+\frac{6C}{r^4}\right)\cos 2\theta \tag{8B}$$

$$\tau_{r\theta} = -\frac{\partial}{\partial r}\left(\frac{1}{r}\frac{\partial\phi}{\partial\theta}\right) = \left(2A+6Br^2-\frac{6C}{r^4}-\frac{2D}{r^2}\right)\sin 2\theta \tag{8C}$$

The constants of integration are now to be determined from conditions of Eq. (2) for the outer boundary and from the condition that the edge of the hole is free from external forces. The conditions give the following:

Table 1 – Comparison among numerical solutions I.

Items	Points					
	[9°S] (9° spacing)			[3°S] (3° spacing)		
	A	B	C	A	B	C
σ_x	0.21	0.09	−0.59	0.11	0.29	−0.84
σ_y	2.35	0.93	0.02	2.75	0.72	−0.02
τ_{xy}	0.00	0.35	0.00	0.00	0.44	0.00
σ_n	2.35	1.06	0.59	2.75	0.99	0.84
	[2°S] (2° spacing)			[2°SF] (full integration)		
	A	B	C	A	B	C
σ_x	0.08	0.34	−0.91	0.02	0.34	−0.99
σ_y	2.85	0.66	−0.02	2.98	0.69	0.02
τ_{xy}	0.05	0.46	−0.01	0.05	0.48	0.04
σ_n	2.86	0.99	0.91	2.98	1.03	0.99
	[1°S] (1° spacing)			[0.5°S] (0.5° spacing)		
	A	B	C	A	B	C
σ_x	0.04	0.41	−0.96	0.02	0.45	−1.00
σ_y	2.94	0.59	−0.01	3.00	0.55	0.0
τ_{xy}	0.0	0.48	0.0	0.0	0.49	0.0
σ_n	2.94	0.99	0.96	3.00	0.99	1.00

Table 2 – Comparison of analytical and numerical results.

Items	Points					
	Analytical solutions			Numerical solutions [0.5°S]		
	A	B	C	A	B	C
σ_x	0.00	0.5	−1.0	0.02	0.45	−1.00
σ_y	3.00	0.5	0.0	3.00	0.55	0.0
τ_{xy}	0.00	0.5	0.0	0.0	0.49	0.0
σ_n	3.00	1.0	1.0	3.00	0.99	1.00

$$2A + \frac{6C}{b^4}+\frac{4D}{b^2} = -\frac{1}{2}S \tag{9A}$$

$$2A + \frac{6C}{a^4}+\frac{4D}{a^2} = 0 \tag{9B}$$

$$2A + 6Bb^2 - \frac{6C}{b^4}-\frac{2D}{b^2} = -\frac{1}{2}S \tag{9C}$$

$$2A + 6Ba^2 - \frac{6C}{a^4}-\frac{2D}{a^2} = 0 \tag{9D}$$

Solving these equations for the problem described in Fig. 3, with $a = 17.5$ mm (inner radius of ducts) and $b = 162.5$ mm, so that $a^2/b^2 = (a/b)^2 = 0.01 \approx 0.0$, we obtain:

$$A = -\frac{S}{4} \quad B = 0 \quad C = -\frac{a^4}{4}S \quad D = \frac{a^2}{2}S$$

Substituting these values of constants into Eq. (8) and adding the stresses produced by the uniform tension ½ S on the outer boundary calculated from Eq. (2), we find that:

$$\sigma_r = \frac{S}{2}\left(1-\frac{a^2}{r^2}\right)+\frac{S}{2}\left(1+\frac{3a^4}{r^4}-\frac{4a^2}{r^2}\right)\cos 2\theta \tag{10A}$$

$$\sigma_\theta = \frac{S}{2}\left(1+\frac{a^2}{r^2}\right)-\frac{S}{2}\left(1+\frac{3a^4}{r^4}\right)\cos 2\theta \tag{10B}$$

$$\tau_{r\theta} = -\frac{S}{2}\left(1-\frac{3a^4}{r^4}+\frac{2a^2}{r^2}\right)\cos 2\theta \tag{10C}$$

If r is very large, σ_r and $\tau_{r\theta}$ approach the values given in Eq. (1).

At the edge of the hole $r = a$, and we find that:

$$\sigma_r = \tau_{r\theta} = 0, \quad \sigma_\theta = S - 2S\cos 2\theta \tag{11}$$

It can be seen that σ_θ is greatest when $\theta = \pi/2$ or $\theta = 3\pi/2$, that is, at the ends m and n of the diameter perpendicular to the direction of the tension in Fig. 4A. At these points, $(\sigma_\theta)_{max} = 3S$. This is the maximum tensile stress and is three times the uniform stress S applied at the ends of the plate.

At points p and q, θ is equal to π and 0, respectively, and we find that:

$$\sigma_\theta = -S$$

so that there is a compression stress in the tangential direction at these points.

For the cross section of the plate through the center of the hole and perpendicular to the y axis, $\theta = \pi/2$, and from Eq. (10),

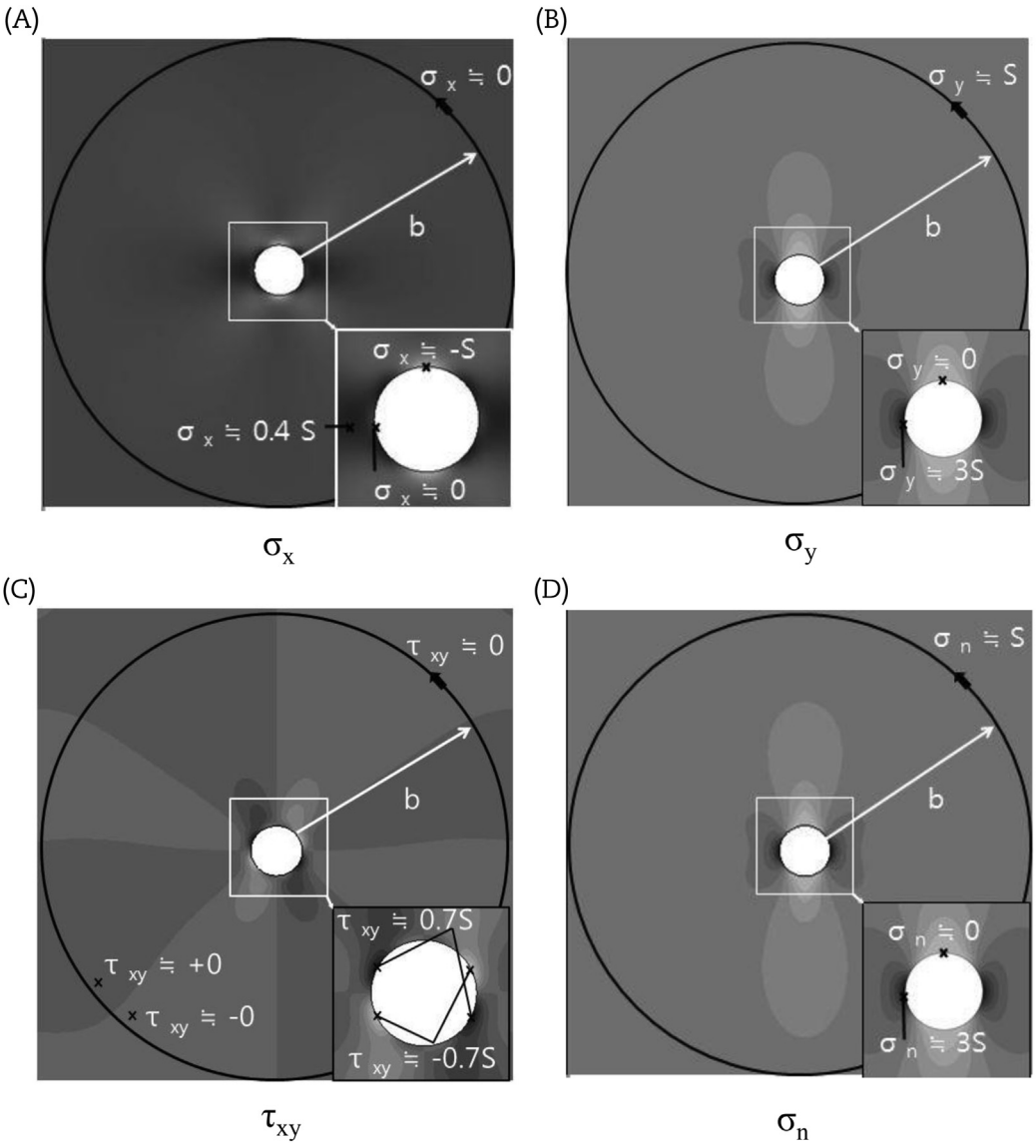

Fig. 6 – Stress contours near the circle of radius *b* [2°S]. (A) σ_x. (B) σ_y. (C) τ_{xy}. (D) σ_n.

$$\tau_{r\theta} = 0, \quad \sigma_\theta = \frac{S}{2}\left(2 + \frac{a^2}{r^2} + 3\frac{a^4}{r^4}\right) \tag{12}$$

The stress distributions according to Eq. (12) are described in Figs. 2–4 with arrows.

It is evident that the effect of the hole is of *a localized character*. Although the stress σ_θ rapidly approaches the value S as *r* increases, the stress concentration near the duct may affect early cracking initiation or expectation of most vulnerable locations all over the structure.

3. Parametric studies

3.1. *Comparison of analytical and numerical solutions*

The analytical solution based on the *theory of elasticity* explained in Section 2.3 is applicable to the typical problem of Fig. 3. However, the geometrical conditions, each material property of structural members in a nonlinear region, and the composite behavior among them are too complex in real structures of PCCVs to be evaluated with analytical approaches only.

Fig. 7 – Typical section of sheathing ducts in a PCCV wall. PCCV, prestressed concrete containment vessel.

Numerical approaches, especially based on the *finite element method*, are very helpful to overcome the limitations of the analytical approach, and to evaluate both local and global behaviors of PCCVs realistically.

It is important to check the property of element type and the size and shape of the generated mesh in the finite element method to get reasonable results. For that reason, numerical simulations for the problem described in Fig. 3 have been performed, and the results of the simulations are compared with the results based on the analytical solution in Section 2.3.

Fig. 5 shows a finite element model and meshes generated for a concrete structure with linear and elastic material properties for simplification. In the model, the height of the structure was five times higher than the height described in Fig. 5 so the simulation would match the assumption in Section 2.3 that the outer radius denoted as b in Fig. 4A is large enough.

The numerical analyses were conducted with ABAQUS version 6.10-1 (Dassault Systèmes, Vélizy-Villacoublay, France). In the process of structural modeling and mesh generation, several factors that may make differences between analytical solutions by Eq. (10) and numerical solutions were nominated as follows: (1) mesh size sensitivity in the finite element method; (2) numerical errors inherent from element type in the finite element method; and (3) assumption of $a^2/b^2 = (a/b)^2 = 0.01 \approx 0.0$, inducing Eq. (10) and b of 325 mm (12.8″), which means that the wall thickness is large enough to meet the assumption in the x direction in the numerical simulation.

To check for the effects of (1), five finite element models of 9°, 3°, 2°, 1°, and 0.5° spacing around a duct hole with reduced integration continuum elements (C3D8R in ABAQUS; Dassault Systèmes), named [9°S], [3°S], [2°S], [1°S], and [0.5°S], respectively, were performed.

An additional finite element model of 2° spacing with full-integration continuum elements (C3D8 in ABAQUS; Dassault Systèmes), named [2°SF], was performed and compared with the case of reduced integration to check for the effects of (2).

To see the effect of (3), the stress contours at the boundary of b for each simulation were checked.

The stresses at points A, B, and C in Fig. 5B by the six numerical simulations are listed in Table 1. The stresses by Eq. (10) based on the *theory of elasticity* and by the numerical simulation of [0.5°S] with fine meshes are listed and compared in Table 2.

The values in Tables 1 and 2 are normalized ones divided by the vertical external uniform stress of S.

The stress components in cylindrical coordinates in Eq. (10) can be transformed to the stress components in rectangular coordinates by Eq. (13).

$$\sigma_x = \sigma_r \sin^2\theta + \sigma_\theta \cos^2\theta + 2\tau_{r\theta} \sin\theta \cos\theta \tag{13A}$$

Table 3 – Material properties of the concrete and sheath.

Items		Value
Concrete	Elastic modulus, GPa (ksi)	27.0 (3,912)
	Poisson ratio	0.18
Sheath	Elastic modulus, GPa (ksi)	219.0 (31,720)
	Poisson ratio	0.3

Table 4 – Comparison among numerical solutions II.

Items	Points					
	[2°SS]			[2°SFS]		
	A	B	C	A	B	C
σ_x	1.00	−0.50	0.02	1.00	−0.57	0.02
σ_y	0.82	1.50	0.16	0.81	1.57	0.15
τ_{xy}	−0.04	−0.08	−0.03	0.04	−0.08	0.03
σ_n	1.00	1.50	0.16	1.00	1.57	0.15
	[0.5°SS]			[0.5°S]		
	A	B	C	A	B	C
σ_x	1.05	−0.55	0.02	0.02	0.45	−1.00
σ_y	0.81	1.54	0.02	3.00	0.55	0.0
τ_{xy}	0.00	−0.08	0.02	0.0	0.49	0.0
σ_n	1.05	1.54	0.04	3.00	0.99	1.00

$$\sigma_y = \sigma_r \cos^2\theta + \sigma_\theta \sin^2\theta - 2\tau_{r\theta} \sin\theta \cos\theta \tag{13B}$$

$$\tau_{xy} = (\sigma_\theta - \sigma_r)\sin\theta \cos\theta + \tau_{r\theta}(\sin^2\theta - \cos^2\theta) \tag{13C}$$

$$\sigma_n = \frac{\sigma_y + \sigma_x}{2} + \sqrt{\left[\frac{(\sigma_y - \sigma_x)}{2}\right]^2 + \tau_{xy}^2} \tag{13D}$$

where σ_x, σ_y: normal components of stress parallel to x and y axes; τ_{xy}: shearing stress in rectangular coordinates; and σ_n: maximum principal stress.

Based on Tables 1 and 2, the gaps between the analytical and numerical solutions get narrower as the element mesh gets denser. For example, stresses in the y direction (σ_y) at point A are 2.35 and 3.00, in the numerical solutions of [9°S] and [0.5°S], respectively, while the value by the analytical solution is 3.00.

In the comparison of analytical and numerical solutions of [0.5°S], very good agreements between them can be seen in Table 2.

Even the differences of σ_x and σ_y at B are relatively high; the differences of maximum principal stresses (σ_n) at all locations are < 0.01%.

Due to the fact that the gaps between the analytical and numerical solutions for σ_x and σ_y at B get narrower as the element mesh gets denser from [9°S] to [0.5°S], a more densely meshed numerical model than [0.5°S] might reduce the gaps.

However, in this study, to check whether the stress concentration near the duct affects early cracking initiation or expectation of most vulnerable locations, maximum principal stresses (σ_n) are the most important factor, which are almost the same by less than 10% for all components at each location for all cases from [2°S] to [0.5°S].

In addition, whether the assumption that the outer radius denoted as b in the analytical solution is large enough is valid in the parametric studies can be checked by the stress contours in numerical simulations.

The stress contours near the circle of radius b in the simulation of [2°S] are displayed in Fig. 6.

Stresses in the y direction (σ_y) and the maximum principal stress (σ_n) are almost equal to S along the circle with a deviation of < 0.5%.

The stresses in the x direction (σ_x) and the shearing stress (τ_{xy}) are nearly equal to 0 along the circle with a deviation of $< \pm 0.01S$.

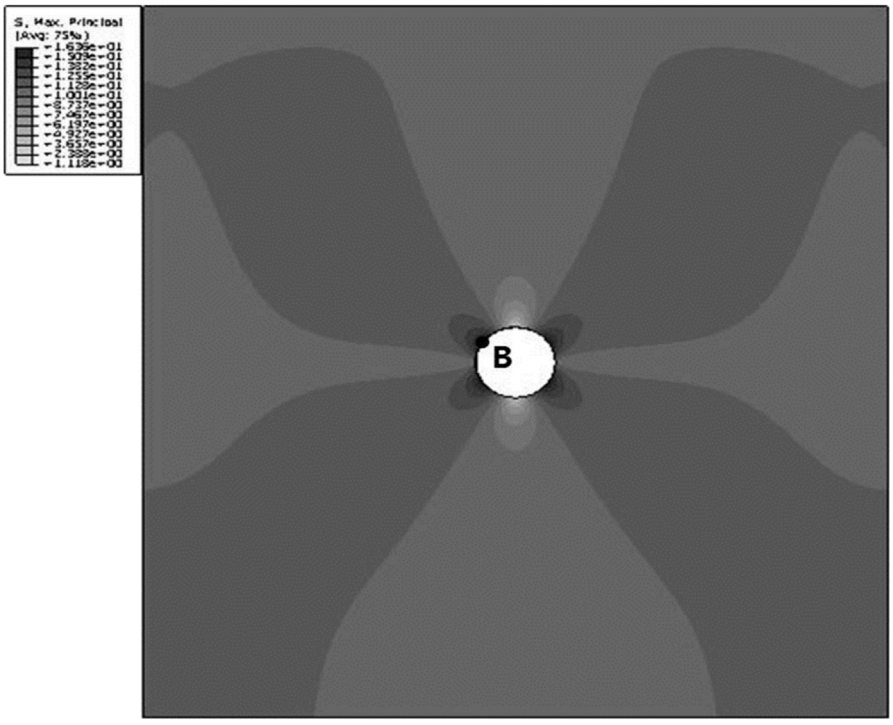

Fig. 8 – Maximum principal stress contour [0.5°SS].

Similar tendencies were obtained in the other cases of [9°S], [3°S], [2°SF], [1°S], and [0.5°S].

Accordingly, the assumption that *b* of 325 mm (12.8″), which is the wall thickness, is large enough is valid in the parametric studies.

3.2. *Effects of sheaths to stress concentration near ducts*

A typical picture of hoop and meridional sheaths for tendons' passing in a PCCV wall section is displayed in Fig. 7. Thet1:4 scale PCCV model tendons were inserted in galvanized metal

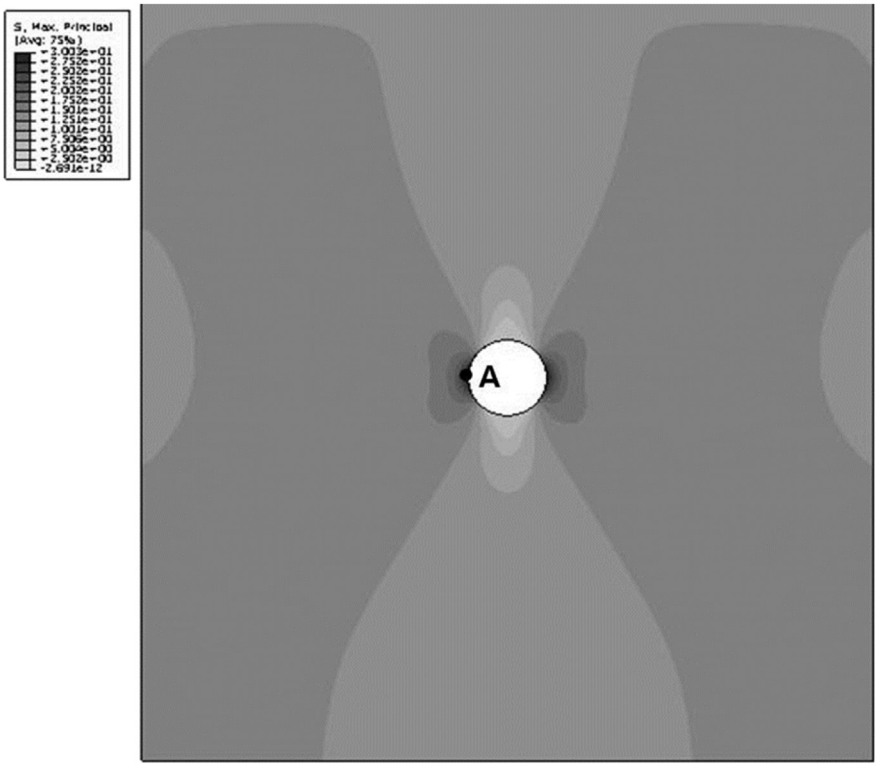

Fig. 9 – Maximum principal stress contour [0.5°S].

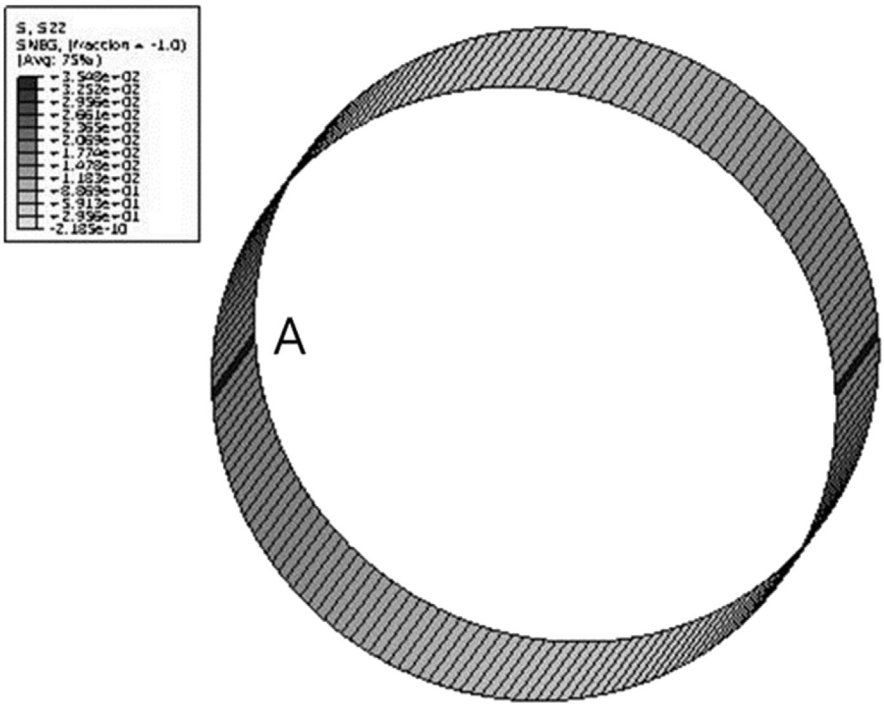

Fig. 10 – Maximum principal stress of sheath [0.5°SS].

sheaths after the concrete had been placed and allowed to cure, and then tensioned.

With regard to the stress concentration phenomenon near ducts, the effects of sheaths need to be verified because they are made of steel, which has structural stiffness.

The nominal thickness of the sheath in the 1:4 scale PCCV model is 3.2 mm (1/8″) and the nominal inner diameter of the sheathing duct hole is 35 mm (1–3/8″).

It is not evident how well the sheaths and concrete behave as a completely unified composite. However, a numerical simulation using the assumption that the completely unified composite between the sheaths and concrete can give the results of the situation in the case the sheaths contribute to the stiffness of wall section as much as possible.

Accordingly, numerical simulations under the assumption of the completely unified composite action between the sheaths and concrete were performed and compared with the results without consideration of sheaths, as in Section 3.1.

The values of material properties used in the numerical simulations, based on the realistic values from the 1:4 scale model test, are listed in Table 3.

Three numerical simulations of [2°SS], [2°SFS], and [0.5°SS] with the same geometrical conditions of the cases of [2°S], [2°SF], and [0.5°S] with the addition of the sheath meshes as shell elements along the hole, respectively, were performed: [2°SS]: 2° spacing, sheath meshed (reduced integration); [2°SFS]: 2° spacing, full integration, sheath meshed; and [0.5°SS]: 0.5° spacing, sheath meshed (reduced integration).

Stresses at points *A*, *B*, and *C* in Fig. 5B by the four numerical simulations [2°SS], [2°SFS], [0.5°SS], and [0.5°S] are listed in Table 4 for comparison.

In the comparison between [0.5°SS] and [0.5°S], with and without consideration of the sheath, respectively, the locations of the highest value of the maximum principal stress are *B* and *A*, respectively.

The maximum principal stress contours of concrete for the cases of [0.5°SS] and [0.5°S] are displayed in Figs. 8 and 9, respectively. The stresses are relatively high in the dark regions and low in the bright regions in Figs. 8 and 9.

The principal stress of concrete at *A* gets reduced from 3.0*S* for [0.5°S] to 1.05*S* for [0.5°SS] with the stiffness contribution of the sheath.

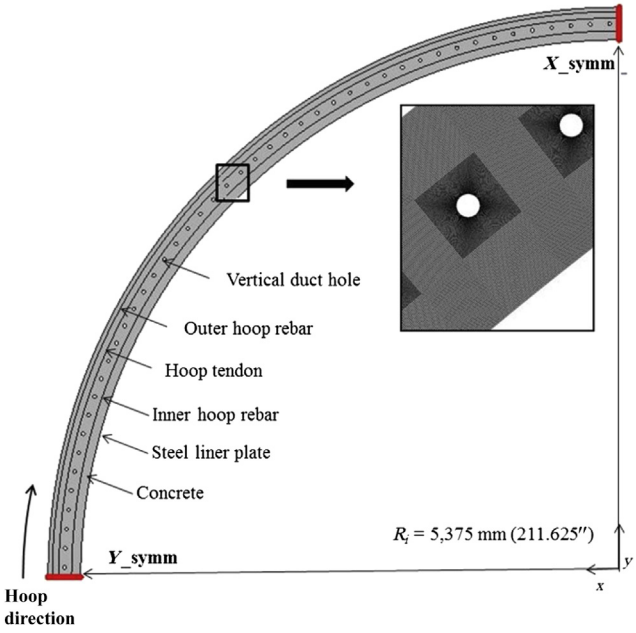

Fig. 11 – A 1/4 symmetric model in hoop direction.

By contrast, the principal stress of concrete at *B* gets increased from 0.99S for [0.5°S] to 1.54S for [0.5°SS] with almost no stiffness contribution of the sheath, as shown in Fig. 10.

The maximum principal stresses of the sheath near point *A* in the dark region are almost 3S but are almost 0.0 at other bright regions, as shown in Fig. 10.

In addition, to meet the compatibility condition at the boundary of the general region, where the stresses are the same as in the plate without the duct hole, somewhere else must be elongated more than others instead of point *A* stiffened by the sheath, which is point *B* for [0.5°SS].

Through the parametric studies, which are not explained specifically in this paper, the higher the stiffness of the sheath gets, the closer to *C* from *A* the point where the maximum principal stress occurs along the periphery of the duct hole in Fig. 5B.

If the stiffness of the sheath becomes much higher than the case of [0.5°SS] in Fig. 8, the maximum principal stress would occur at point *C*, where the stiffness augmentation by the sheath in the vertical direction is the least along the periphery of the duct hole, rather than at point *B* with sufficiently augmented stiffness by the sheath in the vertical direction.

As the maximum principal stress in [0.5°SS], even the case considering the stiffness of sheaths, is 1.54S, which is 54% higher than the normal stress of S without a hole, the effects of the duct hole need to be checked for the behavior of the wall and the whole structure in view of crack initiation and propagation and other phenomena.

4. Effects of duct hole in circumferential direction under pressure loading

4.1. Structural model

4.1.1. Geometry

The geometries of penetrations, prestressing buttresses, nonuniform layout of the prestressing tendons, and reinforcement are too complex to evaluate the effects of parameters on the structural behavior at once in a PCCV.

Accordingly, an axisymmetric approach in the meridional direction and a unit-height simple model approach in the hoop direction are useful for parameter studies and sensitivity analysis.

On these backgrounds, a unit-height simple structural model with 90° segments of an undisturbed part of the 1:4 scale model, including one prestressing tendon, and inner and outer rebars, is considered, as shown in Fig. 11.

Under the assumption of no disturbed geometries of buttress and penetrations for simplicity, the structural behavior subjected to pressure loading along the hoop direction is symmetric in both the x and the y direction, as shown in Fig. 11.

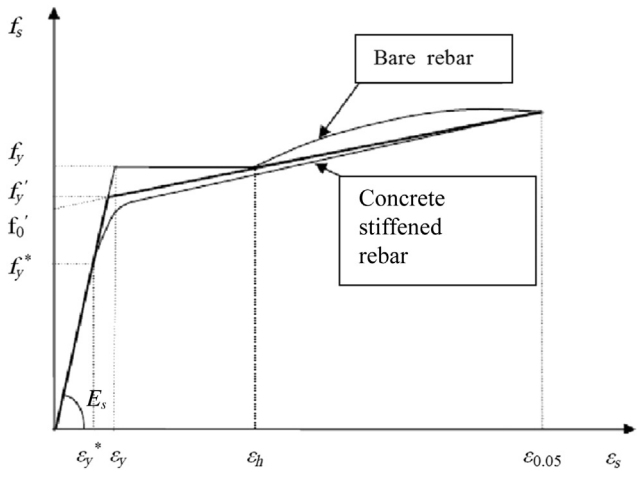

Fig. 12 – Stress–strain relationship of rebar.

4.1.2. Types of elements and contact

The finite element analyses with models of 2° spacing, with the equivalent mesh size of [2°SS] or [2°SFS] in Table 4 both of reduced and full-integration continuum elements (C3D8R and C3D8R in ABAQUS) for concrete were performed. However, the results from the reduced integration and the full integration are not different to be considered seriously, as can be seen in the comparison of [2°SS] and [2°SFS] in Table 4. Therefore, the results of analyses with the reduced integration elements for concrete are discussed in this paper. The steel liner plates with shell elements (S4R in ABAQUS) and rebars and tendon with truss element (T3D2 in ABAQUS) were formulated. In the analysis case considering sheaths, sheaths were formulated with membrane elements (M3D4R in ABAQUS). All nodes of each structural element were rigidly tied or linked.

4.2. Material constitutive models and properties

4.2.1. General

The actual (tested) properties of concrete, reinforcing steel, post-tensioning tendon, and steel liner plate in the 1:4 scale model are referred in the analyses. The properties for these materials are from test data provided by Sandia National Laboratories, Livermore, CA, USA, and used in the construction of the 1:4 scale PCCV at Sandia [2].

Table 5 – Concrete material properties (strengths).

Items	Value
Compressive strength, MPa (psi)	47.3 (6,860)
Tensile strength, MPa (psi)	3.45 (500)

Table 6 – Rebar material properties.

Items	Values [D19 (SD390)]
Elastic modulus, GPa (ksi)	184.0 (26,690)
Poisson's ratio	0.3
Yield stress, MPa (psi)	473.1 (68,600)
Tensile stress, MPa (psi)	658.3 (95,480)
Extension, %	21.1

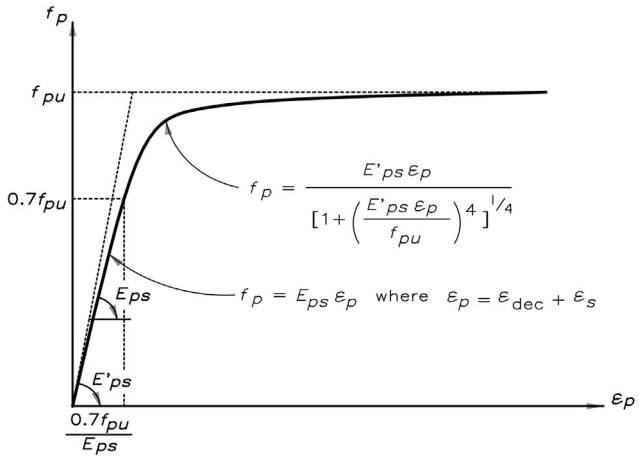

Fig. 13 – Stress–strain relationship of prestressing tendon.

4.2.2. *Concrete*

The concrete is characterized by a materially nonlinear deformation behavior. The material nonlinearity is assumed to occur due to cracking of concrete in tension and plasticity of concrete in compression. However, the material nonlinearity due to the latter has relatively less influence than that due to the former on the failure mode of the containment structure under internal pressure.

The Menetrey–Willam's failure model and modified Drucker–Prager's model with a nonassociated plastic flow that is known to be suitable to represent the tensile concrete cracking of the finite element model are introduced in the numerical analyses [7]. The yield surface and flow potential parameters for an elastoplastic material in the Menetrey–Willam's failure model with nonassociated plastic flow and the strain hardening are defined by the model parameters *r*-factor, friction angle β, and dilation angle ψ. The elliptic function $r(\theta,e)$ controls the shape of the yield surface in the deviatoric plane and angle β is the angle between the yield surface and the pressure stress axis in the meridian plane [8].

In the modified Drucker–Prager's failure model, the yield surface and flow potential parameters for an elastoplastic material are defined by setting the model parameters such as the *K*-factor, the friction angle β, and the dilation angle ψ [9]. Tension stiffening effects are represented in two aspects: one is to modify the stiffness of reinforcing bars embedded in concrete and the other is to modify the stiffness of the concrete [10].

The concrete strengths from the uniaxial strength test data of the trial mix concrete of the 1:4 scale PCCV model listed in Table 5 are used with the other material properties in Table 3.

Table 7 – Tendon material properties.

Items	Values
Elastic modulus, GPa (ksi)	191.0 (27,700)
Elastic limit stress, MPa (psi)	1,339 (194,200)
Yield strength, MPa (psi)	1,691 (245,260)
Poisson's ratio	0.3
Ultimate strength, MPa (psi)	1,912 (277,300)
Extension, %	4.5

4.2.3. *Reinforcement steel (rebar)*

Rebar materials are generally incompressible when they deform plastically and their yielding is independent of the pressure stress. The von Mises failure criterion is used for this steel material. Hsu [11] noted that the stress–strain curves for a bare steel bar and for a steel bar embedded in concrete are quite different, as shown in Fig. 12. Therefore, the stress–-strain relationship of rebar embedded in concrete has been used in the reinforced concrete structure to simulate the realistic behavior of the rebar in concrete.

The stress–strain curve of the rebar for the numerical analysis is idealized by a bilinear curve with a slope of E_s before yielding and a slope of E_p after yielding, as illustrated in Fig. 12. The equations of two lines are expressed at the stress level designated by f_y at which the two straight lines intersect, as shown in Eqs. (14A) and (14B). The plastic modulus E_p' after yielding can be taken as a small fraction of the elastic modulus E_s.

$$f_s = E_s\varepsilon_s \quad \text{for } f_s \le f_y' \tag{14A}$$

$$f_s = f_o' + E_p'\varepsilon_s \quad \text{for } f_s > f_y' \tag{14B}$$

where f_o' is the vertical intercept of the postyield straight line.

The intersection stress level f_y' and the plastic modulus E_p' depend mainly on the level of the apparent yield stress f_y^* illustrated in Fig. 12. The apparent yield stress ratio f_y^*/f_y is sensitive to reinforcement ratio ρ and the solution can be expressed as an average equation [Eq. (15A)], where f_{cr} is the cracking strength of concrete. The values of f_y' and E_p' in the stress–strain relationship used in the numerical analysis are calculated as Eqs. (15B) and (15C) using the apparent yield stress f_y^* and the strain-hardening modulus of the bare bar E_p from the actual material properties.

$$\frac{f_y^*}{f_y} = 1 - \frac{4}{\rho}\left(\frac{f_{cr}}{f_y}\right)^{1.5} \tag{15A}$$

$$\frac{f_y'}{f_y} = 0.43 + 0.5\frac{f_y^*}{f_y} \tag{15B}$$

$$\frac{E_p'}{E_p} = 3.3 - 2.5\frac{f_y^*}{f_y} \tag{15C}$$

The test results provided in the Appendix of Noh et al.'s [4] paper are used in the numerical modeling of the rebar material properties. Table 6 presents the modulus of elasticity for D19 (SD390)-type reinforcement steel, which is considered in the numerical modeling.

Table 8 – Steel liner material properties.

Items	Values
Elastic modulus, GPa (ksi)	219.0 (31,720)
Yield strength, MPa (psi)	376.0 (54,530)
Poisson's ratio	0.3
Ultimate tensile strength, MPa (psi)	499.0 (72,730)

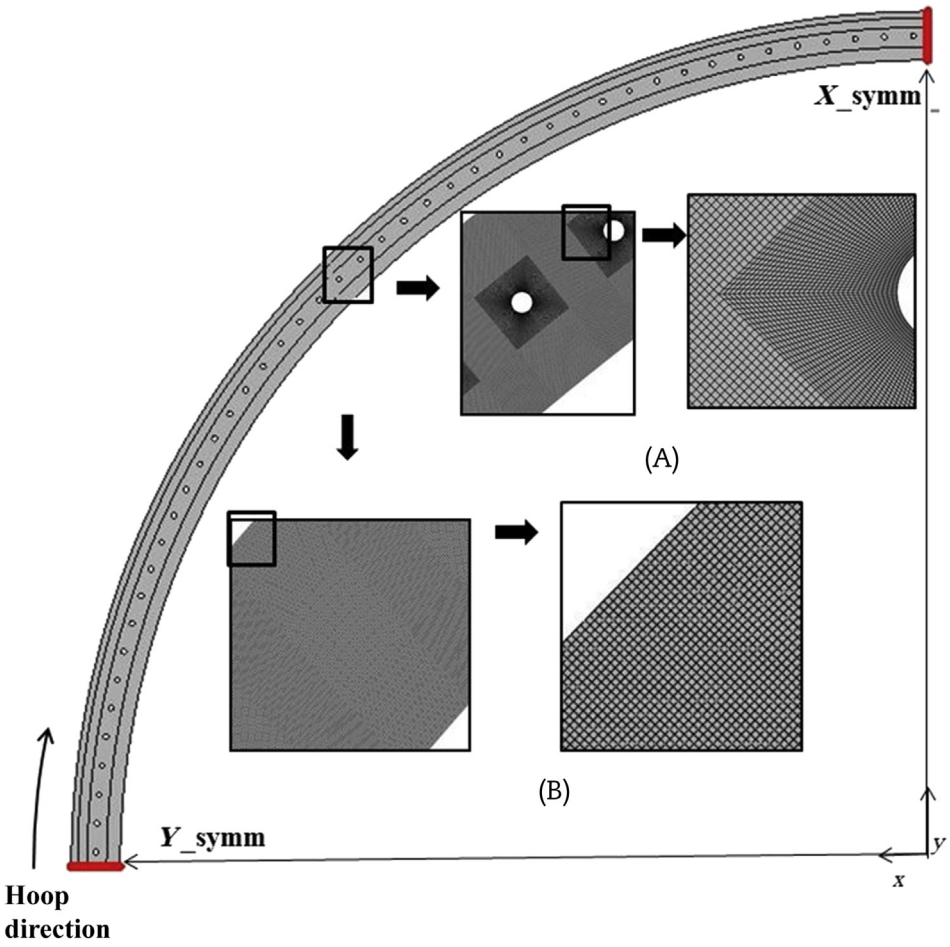

Fig. 14 – Concrete mesh generation for each analysis.

4.2.4. *Prestressing tendon*

The stress–strain curve of a bare prestressing tendon comprising two straight lines joined by a knee curve, as shown in Fig. 13, is used in the numerical analysis. The first part of the curve is a straight line up to $0.7f_{pu}$ and the second part is expressed by the Ramberg–Osgood equation [Eq. (16)] that meets the first part at the stress level of $0.7f_{pu}$.

$$f_p = \frac{E'_{ps}\varepsilon_p}{\left[1+\left(\frac{E'_{ps}\varepsilon_p}{f_{pu}}\right)^4\right]^{1/4}} \tag{16}$$

where f_{pu}, f_p, E_{ps}, and ε_p are the ultimate strength of the tendon, strength of the tendon, tangential modulus Ramberg–Osgood curve at zero load, and sum of strain in the tendon, respectively [11].

The material properties listed in Table 7 are used for modeling the tendon.

4.2.5. *Steel liner plate and sheath*

The stress–strain behavior of the liner plate steel is modeled by using an elastoplastic model. Avon Mises failure surface with kinematic hardening is used to represent the nonlinear behavior of the material.

The material properties of the liner plate used in the numerical analyses are shown in Table 8.

The material properties and failure criteria of the liner plate were assumed to be the same as those for the sheath in the numerical analyses owing to the restricted information about the sheath [2].

4.3. *Analysis results*

Three analyses have been performed: (1) NDH: no duct hole; (2) DH_NS: duct hole with no sheath; and (3) DH_WS: duct hole with sheath.

For the analyses of DH_NS and DH_WS, duct holes were considered in the geometry with the mesh pattern, as shown in Fig. 14A. In the case of DH_WS, the sheath along the periphery of the duct hole was added with membrane elements and nodes rigidly linked to the adjacent nodes of concrete elements.

For the analysis of NDH, the duct hole was not considered in the geometry with the mesh pattern, as shown in Fig. 14B.

A maximum internal pressure of 1.65 MPa (240 psig) was loaded for each analysis.

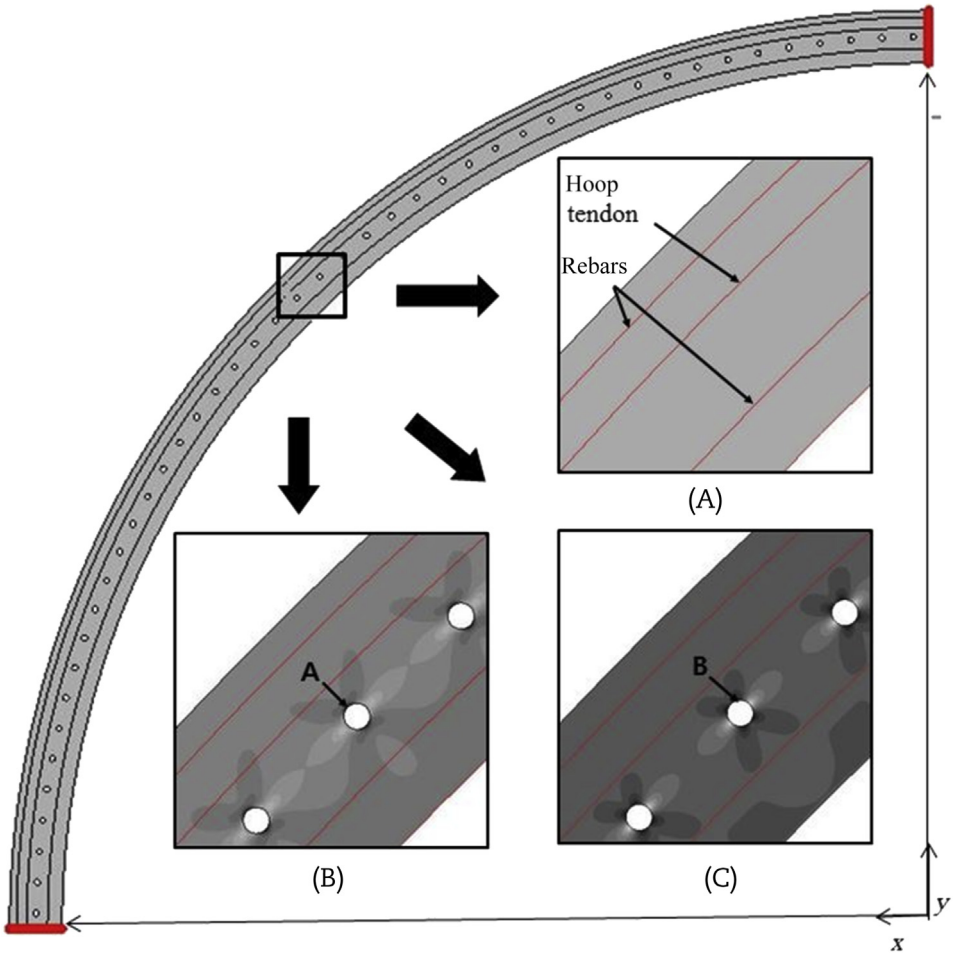

Fig. 15 – Maximum principal stress contours at 1.15P_d. (A) NDH. (B) DH_NS. (C) DH_WS. DH_NS, duct hole with no sheath; DH_WS, duct hole with sheath; NDH, no duct hole.

The maximum principal stress contours of concrete for the cases of NDH, DH_NS, and DH_WS subjected to the SIT pressure of 1.15P_d (57 × 1.15 = 65.6 psig, 0.45 MPa) are displayed in Figs. 15A, 15B, and 15C, respectively. The stresses are relatively high in the dark region and low in the bright region in Fig. 15.

The maximum principal stresses of concrete in the case of NDH through the wall thickness are almost equal, with less than 5% differences.

By contrast, the maximum principal stresses of concrete at point *A* in DH_NS and at point *B* in DH_WS are 270% and 165% larger than the average stresses through the wall thickness, which can be explained with the consistent tendencies discussed in Section 3.2.

Although the maximum stress levels of concrete in Fig. 15 are still in the linear and elastic regions, those can give hints on where the cracks of concrete initiate in advance in nonlinear regions. For example, at the locations of *A* in DH_NS and *B* in DH_WS, the first cracks of concrete might be initiated.

In addition, the fact that the stress contours of concrete near the inner face of the wall are darker, which means higher stresses, than the outer face of the wall in DH_WS is a point of observation for crack propagation in nonlinear regions. This phenomenon can be comprehended with the fact that the inner face is more affected by the loss of stiffness due to the duct hole than the outer face, where the stiffness is relatively higher than the inner face with hoop tendons of high stiffness, to meet the compatibility condition.

The maximum principal stress contours of concrete with cracking regions for the cases of NDH, DH_NS, and DH_WS under 2.0P_d (57 × 2.0 = 114.0 psig, 0.79 MPa) are displayed in Figs. 16A, 16B, and 16C, respectively.

In the comparison of NDH, DH_NS, and DH_WS, the cracking regions are of main concern, which affect the deformation of the steel liner plates.

In the case of NDH, the concrete cracking regions at 2.0P_d are concentrated between the outer rebar and the hoop tendon far from the steel liner plates.

The concrete cracking regions are distributed near the duct holes and near the steel liner plates in the cases of DH_NS and DH_WS, which induce large deformations of the steel liner plates.

The pressure levels for several weighty statuses from each analysis are summarized in Table 9.

The pressure levels to reach initial concrete crack, yielding of steel liner plates, and yielding of rebar in DH_WS are

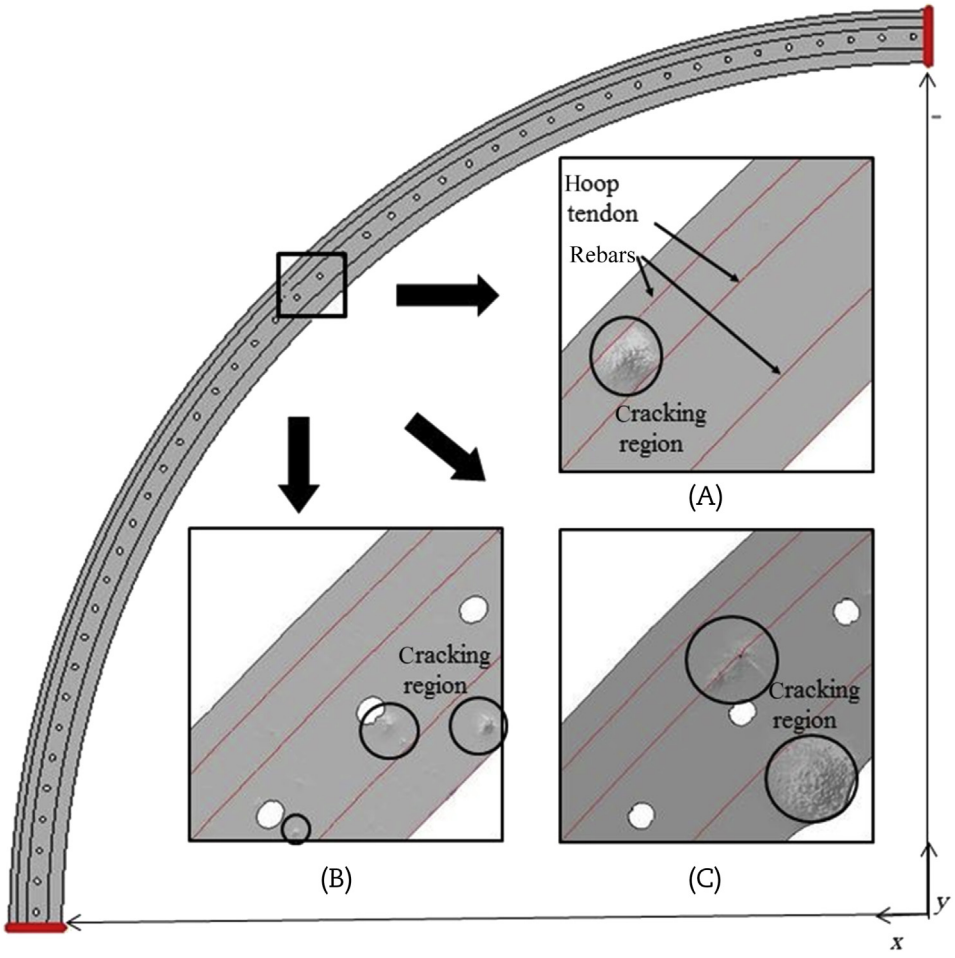

Fig. 16 – Maximum principal stress contours at 2.0P_d. (A) NDH. (B) DH_NS. (C) DH_WS. DH_NS, duct hole with no sheath; DH_WS, duct hole with sheath; NDH, no duct hole.

slightly lower than those in NDH by 12%, 1%, and 0.4% and those in DH_NS by 11%, 1%, and 0.1%, respectively.

Conversely, the pressure levels to reach liner rupture of 1% strain in DH_NS and DH_WS (both under consideration of duct hole) are considerably lower (by 46%) than that in NDH (without consideration of duct hole).

Owing to the importance of leak tightness of the steel liner plates, the results are so significant that the effects of no stiffness inside unbonded tendon ducts should not be ignored, but be considered properly in the numerical simulation of a PCCV under internal pressure loading.

Table 9 – Comparisons of pressure levels (MPa).

Status	NDH	DH_NS	DH_WS
Initial concrete crack	0.745	0.739	0.668
Yielding of steel liner plates	0.739	0.738	0.730
First yield of hoop rebar	1.18	1.14	1.13
Steel liner 1% strain	1.10	0.75	0.75
Tendon yielding	1.30	1.43	1.35

DH_NS, duct hole with no sheath; DH_WS, duct hole with sheath; NDH, no duct hole.

5. Summary and conclusion

(1) The walls of a PCCV under internal pressure loadings are submitted to biaxial tension in circumferential and meridional directions, in general.
(2) The geometrical conditions of walls in a PCCV containing meridional tendon duct holes under circumferential tension belong to the problem plates with a circular hole under one-directional tension.
(3) Based on the theoretical background of *the theory of elasticity*, stress concentration effects and stress distribution along the periphery of duct holes were analytically obtained.
(4) Several parametric numerical simulations were performed, and their results are compared with those from the analytical approach. The results from the numerical approach were almost the same as those from the analytical approach, especially in densely meshed cases.
(5) Using the numerical approach, which is consistent with the analytical approach with linear and homogeneous material properties, three cases of nonlinear analyses under high internal pressure for a unit-height simple

structure based on the 1:4 scale PCCV model have been performed.

(6) The constitutive models of the material introduced here were confirmed to be able to avoid numerical instability up to $3.5P_d$ of the 1:4 scale PCCV model.

(7) In the comparison of concrete cracking patterns under $2.0P_d$, the cracking regions of two cases considering duct holes (DH_NS and DH_WS) are mainly distributed near the steel liner plates, but those of the other case not considering duct holes (NDH) are distributed far from liners.

(8) The pressure levels to reach liner rupture of 1% strain in DH_NS and DH_WS (both under consideration of duct holes) are considerably lower (by 46%) than that in NDH (without consideration of duct holes); therefore, the effects of duct holes should be considered for structural integrity evaluation of a PCCV.

6. Further study

(1) The meridional behavior considering hoop tendon ducts and the coincident triaxial behaviors considering hoop and meridional tendon ducts need to be studied; however, only the circumferential behavior considering meridional tendon ducts were mainly focused on in this paper.

(2) A simplified but reasonable numerical approach, with a considerably denser element mesh than those used in this work, needs to be studied to consider the effects of duct holes on the whole behavior in a PCCV with complex geometries of penetrations, prestressing buttresses, nonuniform layout of the prestressing tendons, and reinforcement.

(3) Various parametric studies of constitutive models for concrete and other materials, modeling methodologies of unbonded tendons, element type and size effects, and the connection conditions of structural elements may result in more consistent effects of duct holes on the behavior of PCCVs than those discussed in this paper.

Conflict of interest

The authors declare no conflict of interest.

Acknowledgments

This work was financially supported by the Research and Development Program of the Korea Institute of Energy Technology Evaluation and Planning funded by the Ministry of Trade, Industry and Energy (MOTIE; No. 201451010169B).

REFERENCES

[1] R.Y. Jung, H.I. Cho, S.M. Ahn, The Structural Integrity Test for the Shin-kori Unit 3 Containment and Acceptance Criteria, Transactions, SMiRT-22 Division VI, 2013.

[2] M.F. Hessheimer, E.W. Klamerus, L.D. Lambert, G.S. Rightley, Overpressurization Test of a 1:4–Scale Prestressed Concrete Containment Vessel Model, NUREG/CR-6810, SAND2003-0840P, Sandia National Laboratories, Livermore (CA), 2003.

[3] R.A. Dameron, B.E. Hansen, D.R. Parker, Y.R. Rashid, Post-test Analysis of the NUPEC/NRC 1:4 Scale Prestressed Concrete Containment Vessel Model, NUREG/CR-6809, SAND2003-0839P, Sandia National Laboratories, Livermore (CA), 2003.

[4] S.H. Noh, R.Y. Jung, S.T. Kim, S.J. Lim, The Structural Integrity Test for a PSC Containment with Unbonded Tendons and Numerical Analysis I, vol. 28, No. 5, Computational Structural Engineering Institute of Korea, 2015, pp. 523–533.

[5] S.H. Noh, R.Y. Jung, B.S. Lee, S.J. Lim, The Structural Integrity Test for a PSC Containment with Unbonded Tendons and Numerical Analysis II, vol. 28, No. 5, Computational Structural Engineering Institute of Korea, 2015, pp. 535–542.

[6] S.P. Timoshenko, J.N. Goodier, Theory of Elasticity, McGraw-Hill, Singapore, 1970.

[7] S. Smith, On Fundamental Aspects of Concrete Behavior, MSc Thesis, University of Colorado, Boulder (CO), 1987.

[8] P.H. Menetrey, K.J. Willam, Triaxial failure criterion for concrete and its generation, ACI Struct. J. 92 (1995) 311–318.

[9] W.F. Chen, Constitutive Equations for Engineering Materials, Elsevier, Philadelphia (PA), 1994.

[10] H. Okamura, K. Maekawa, Nonlinear Analysis and Constitutive Models of Reinforced Concrete, Kibodang, 1990.

[11] T.T.C. Hsu, Unified Theory of Reinforced Concrete, CRC Press, 1993, pp. 205–218.